Hedgehog spin texture and Berry's phase tuning in a magnetic topological insulator

Su-Yang Xu, M. Neupane, Chang Liu, D. M. Zhang, A. Richardella, L. A. Wray,

N. Alidoust, M. Leandersson, T. Balasubramanian, J. Sánchez-Barriga,

O. Rader, G. Landolt, B. Slomski, J. H. Dil, J. Osterwalder, T.-R. Chang,

H.-T. Jeng, H. Lin, A. Bansil, N. Samarth, and M. Z. Hasan

This file includes:

Fig. S1 to S21

SI I. Materials and methods

Spin-integrated angle-resolved photoemission spectroscopy (ARPES) measurements were performed with 29 eV to 64 eV photon energy on beamlines 10.0.1 and 12.0.1 at the Advanced Light Source (ALS) in Lawrence Berkeley National Laboratory (LBNL). Spin-resolved ARPES measurements were performed on the I3 beamline at Maxlab [1, 2] in Lund, Sweden, COPHEE spectrometer SIS beamline at the Swiss Light Source (SLS) in Switzerland [3, 4], and UE112-PGM1 beamline PHOENEXS chamber at BessyII in Berlin, Germany, using the classical Mott detectors and photon energies of $8-11$ eV, $20-22$ eV, and $55-60$ eV for the three beamlines respectively. For ARPES measurements, samples were decapped *in situ* to prepare the clean surface (see below), and measured at temperature below 50 K at chamber pressure less than 2×10^{-10} torr at all beamlines.

The Mn doped Bi_2Se_3 thin films were synthesized by Molecular Beam Epitaxy (MBE) using high purity elemental (5N) Mn, Bi, and Se sources. A thin GaAs buffer layer was first deposited on the epi-ready GaAs 111A substrate after thermal desorption of the native oxide under As pressure. Then the substrate was transferred to another chamber without breaking the vacuum, where a second buffer layer of ZnSe was deposited to further smooth the surface. Mn-Bi_2Se_3 layer (~ 60 nm) was then grown with a high Se/Bi beam equivalent pressure (BEP) ratio of ~ 15. The Mn doping concentration was controlled by adjusting the Bi/Mn BEP ratio ranging from 8 to 60. To protect the surface from oxidation, a thick Se capping layer was deposited on the Mn-Bi_2Se_3 thin film immediately after the growth (see Fig. S1a). The Zn doped Bi_2Se_3 control samples were also synthesized under the same conditions as Mn-Bi_2Se_3, with the Zn doping concentration controlled by Bi/Zn BEP. Ultra-thin Bi_2Se_3 film was prepared in thickness of 3 QL, with a typical 1 QL peak to peak variation ($2-4$ QL).

In order to reveal the clean Bi_2Se_3 surface needed for photoemission measurements, the MBE-grown thin films are heated up inside the ARPES chamber to ~ 250°C under vacuum better than 1×10^{-9} torr to blow off the Se capping layer on top of the Bi_2Se_3 film. Fig. S1b demonstrates the decapping process by ARPES core level spectroscopies measurement. Only selenium core level is observed before the decapping process (blue curve), whereas both selenium and bismuth peaks are shown after the decapping (red curve). ARPES measurements are then performed on the clean thin film surface. Fig. S1c-d show a typical spin-integrated
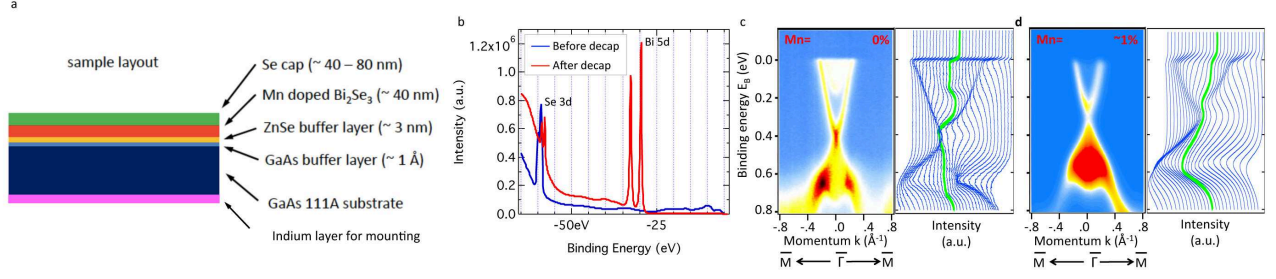
FIG. S1: **Demonstration of sample surface preparation (decapping) procedure in ARPES measurements. a,** Sample layout of the MBE grown Mn(Zn)-doped Bi_2Se_3 films. **b,** Core level spectroscopies on MBE thin film before and after the decapping procedure. **c-d,** typical spin-integrated ARPES dispersion mapping and corresponding energy dispersion curves (EDCs) of undoped and $\sim 1\%$ Mn-doped (nominal concentration) Bi_2Se_3 thin film along high symmetry $\bar{M} - \bar{\Gamma} - \bar{M}$ direction.

ARPES measured dispersion mappings after decapping of both undoped Bi_2Se_3 and $\sim 1\%$ (nominal concentration, same as the maintext) Mn-doped Bi_2Se_3 thin film.

SR-ARPES measurements are performed with double Mott detector setup, which enables to measure spin-resolved photoemission spectra along momentum $k_{//}$ at fixed binding energy E_B (SR-MDC) or along binding energy E_B at fixed momentum $k_{//}$ (SR-EDC) for all three spatial directions ($I\hat{x}\uparrow\downarrow$, $I\hat{y}\uparrow\downarrow$, and $I\hat{z}\uparrow\downarrow$). The detailed and comprehensive review of SR-ARPES technique is presented in Ref. [5]. The spin-resolved data on Mn-Bi_2Se_3 shown in the main paper is done in remanent magnetization mode: the film is pre-magnetized in the UHV preparation chamber in the ARPES system at the base temperature by approaching the film with a permanent magnet with magnetic field roughly at 0.4T, in order to induce the remanent magnetization. The film is then transferred from the preparation chamber to the measurement chamber to perform spin-resolved measurements, maintaining the pressure and temperature.

The surface sensitivity of ARPES measurements can be obtained from the photoemission electron escape depth. As shown in Fig. S2, the electron escape depth with incident photon energy from $(50 - 60 \text{ eV})$ are well below 5 Å. This is important to explain the SR-ARPES data on the ultra-thin 3 QL Bi_2Se_3 in the maintext, because a within Å escape depth of the photoelectron means SR-ARPES probes the very top quintuple layer of the 3 QL film, whose total thickness is around 28.6 Å.
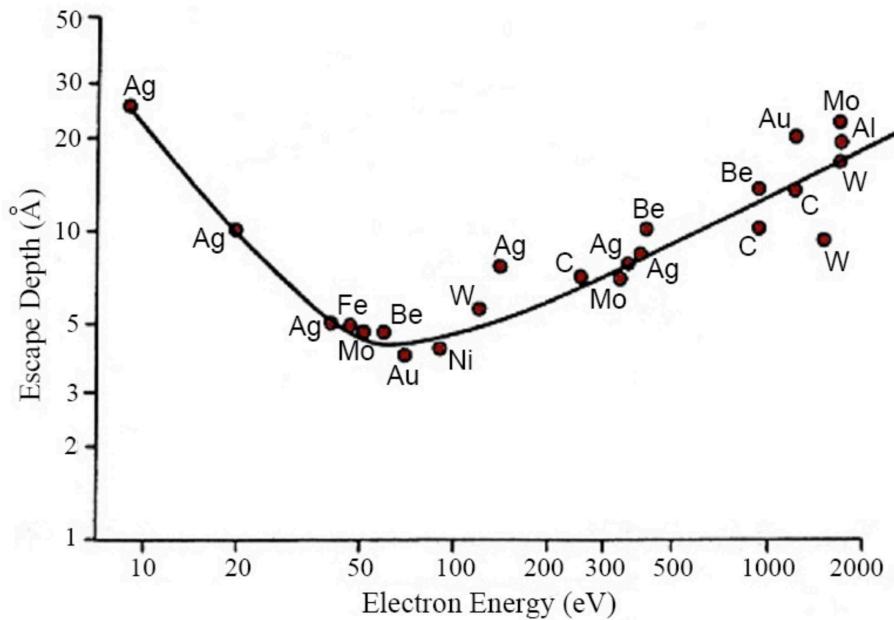
3

FIG. S2: **Universal penetration depth of photoemission electrons.**

Magnetization of the surface in the presence of Mn atoms are checked with X-ray magnetic circular dichroism (XMCD) using total electron yield (TEY) mode that greatly enhances the surface sensitivity (within 50 Å) of the magnetization measurements. XMCD measures the dichroism signal of the L_{23} absorption edge spectra, which is widely used to study the magnetic properties of transition metals and dilute magnetic semiconductor thin films or monolayers. The X-ray magnetic circular dichroism (XMCD) measurements are performed at the back-endstation of D1011 beamline at Maxlab in Lund, Sweden with total electron yield (TEY) mode on Mn-Bi$_2$Se$_3$ film. The temperature of the XMCD measurements ranges from 40 K to 300 K. The magnetic field is applied in the out-of-plane direction normal to the sample surface, with a maximum H field of 300 oe. The left (right) hand circularly polarized incident light is also normal to the film surface, with an accuracy of the circular polarization better than 90%. The sample is prepared the same way as in ARPES measurements *in situ* by decapping inside the XMCD UHV chamber. The XMCD technique and the XMCD measurements on Mn-Bi$_2$Se$_3$ film surface are discussed in detail in the section below SI. II. 3.

Adsorption of NO$_2$ molecules on sample surface was achieved via controlled exposures to NO$_2$ gas (Matheson, 99.5%). The adsorption effects were studied under static flow mode by

4

exposing the clean sample surface to the gas for a certain time at the pressure of 1×10^{-8} torr, then taking data after the chamber was pumped down to the base pressure. Spectra of the NO_2 adsorbed surfaces were taken within minutes of opening the photon shutter to minimize potential photon induced charge transfer and desorption effects.

The first-principles calculations are based on the generalized gradient approximation (GGA) [6] using the full-potential projected augmented wave method [7] as implemented in the VASP package [8]. A $2 \times 2 \times 6$ quintuple-layer slab model with a vacuum thickness lager than 10 Å is used in this work. To simulate the dilute Mn doping, one Bi atom is substituted by one Mn atom in both the top and bottom layers with the internal atomic coordinates optimized. The electronic structure calculations were performed over $5 \times 5 \times 1$ Monkhorst-Pack k-mesh with the spin-orbit coupling included self-consistently.

SI II. Mn-Bi$_2$Se$_3$

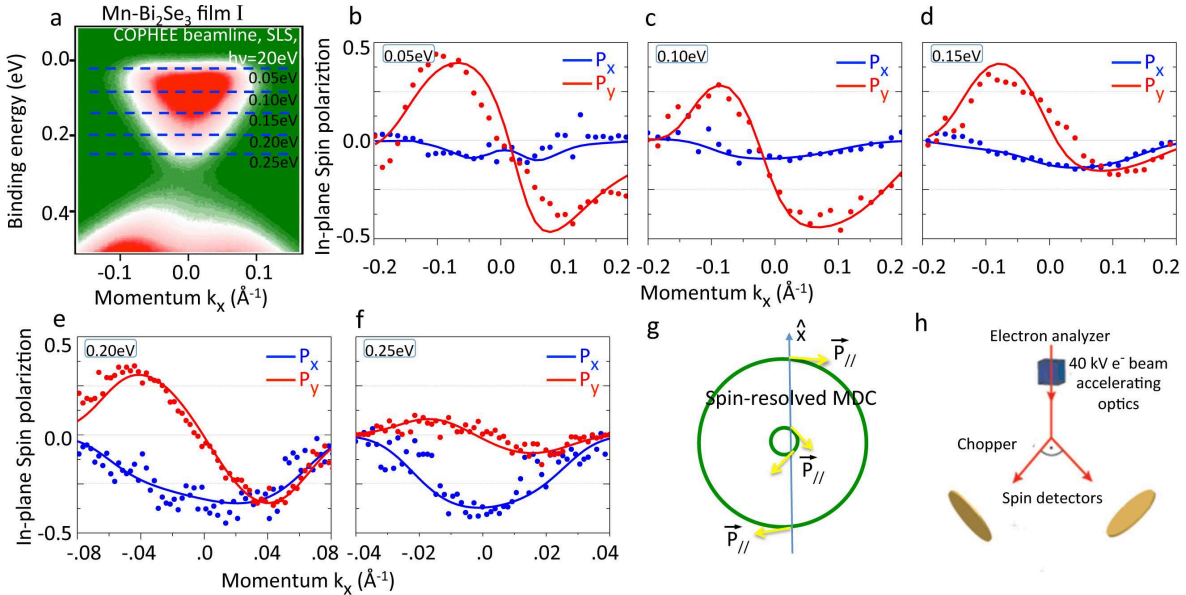### 1. Comprenhensive spin-resolved measurements

FIG. S3: **In-plane spin measurements of Mn-Bi$_2$Se$_3$ film I. a,** Spin-integrated ARPES dispersion mapping at incident photon energy 20 eV (used for spin-resolved measurements). **b-f,** In-plane spin polarization along $\hat{x}$ and $\hat{y}$ directions. **g,** The $\hat{x}$ direction is defined as along the spin-resolved MDC measurement direction.

Here we show comprehensive spin-resolved data on Mn-Bi$_2$Se$_3$ film I and II in the maintext Fig. 3. Mn-Bi$_2$Se$_3$ film I is measured using the COPHEE spectrometer SIS beamline at the Swiss Light Source (SLS) in Switzerland (Fig. S3h) [3, 4]. The measurements are performed in spin-resolved momentum distribution curve (MDC) mode (along momentum, with fixed energies, as shown in Fig. S3a). Since the out-of-plane component is already presented in the maintext (Fig. 3a-d), here we show the in-plane components of the spin-resolved measurements.

The $\hat{x}$ direction is defined as along the spin-resolved MDC measurement direction. Therefore, if the SR-MDC measurements perfectly cross the Brillouin zone (BZ) center $\bar{\Gamma}$ point, then polarization along $\hat{x}$ direction P$_x$ should be strictly zero, whereas P$_y$ should be opposite at the opposite side of the Fermi surface representing the helical spin texture [9]. Fig. S3b-f show the measured in-plane spin polarization along both $\hat{x}$ and $\hat{y}$ directions. Indeed, P$_y$ reverses its sign when going from $-k$ to $+k$. Meanwhile, a finite P$_x$ is also observed which becomes increasingly significant when going to large binding energies close to the Dirac point. Such nonzero P$_x$ is owning to a small tilt of the sample, which results in a "miss-cut" away from the BZ center $\bar{\Gamma}$ point (see Fig. S3g). The observed P$_y$ (opposite sign at opposite sides of the Fermi surface) and P$_x$ (same sign at opposite sides of the Fermi surface) proves that the in-plane components of the spin texture still preserve the helical spin configuration.

Mn-Bi$_2$Se$_3$ film II is measured at the I3 beamline at Maxlab [1, 2] in Lund, Sweden, with the spin-resolved energy distribution curve (EDC) mode (along binding energy, with fixed momenta). The in-plane and out-of-plane measurements are shown in Fig. S4 and Fig. S5 respectively. Since manipulator of the I3 beamline is equipped with an additional motor to tilt the sample, the small tilt due to sample mounting is corrected before measurements. As a result P$_x$ is zero in the measurements. Again, P$_y$ shows the "classical" helical spin texture. Moreover, P$_z$ shows the singly degenerate Dirac point and the TR breaking evidence, which has been presented in the maintext already.
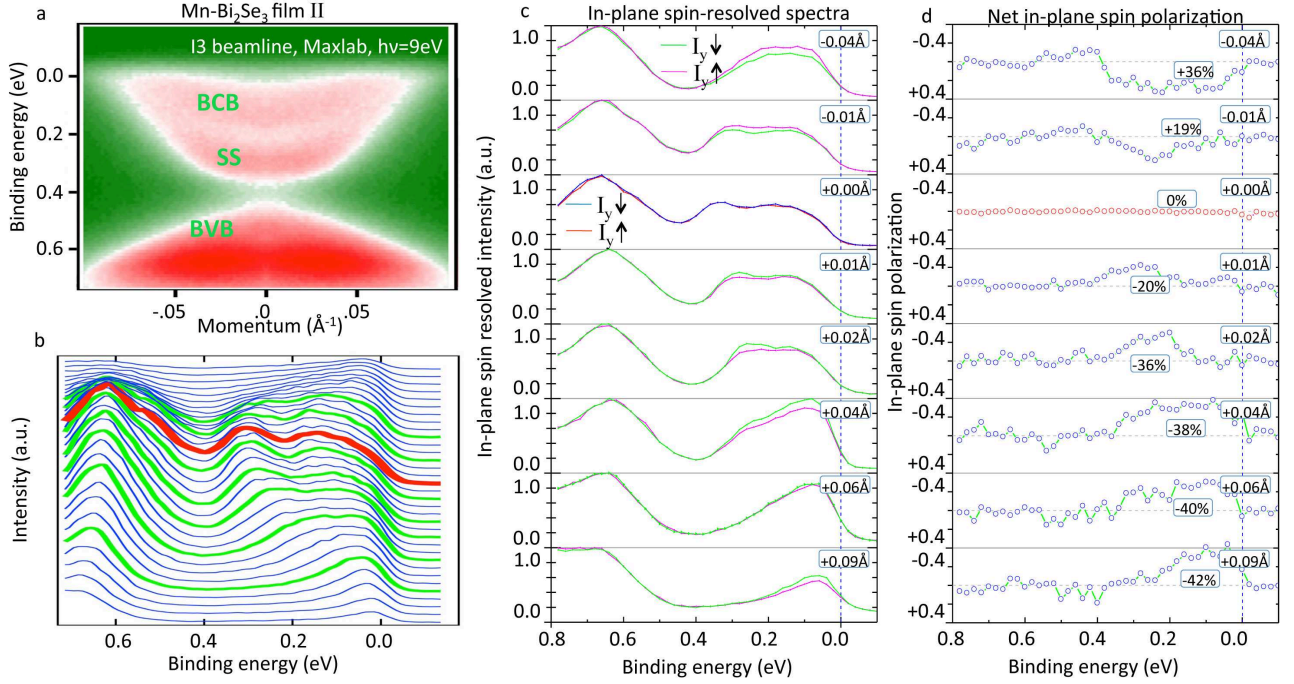
6

FIG. S4: **In-plane spin measurements of Mn-Bi$_2$Se$_3$ film II. a-b,** Spin-integrated ARPES measured dispersion and EDCs with incident photon energy 9 eV (used for spin-resolved measurements). The EDCs selected for spin-resolved measurements are highlighted in green (red) colors in the EDC panel. The EDC at the $\bar{\Gamma}$ momenta is in red color. **c,** In-plane spin-resolved EDC spectra. **d,** In-plane spin polarization obtained from **c.**

2. **Surface magnetic interaction strength b_z based on spin-resolved measurements on Mn-Bi$_2$Se$_3$**

Here we show the details of the method of fitting the magnetic interaction strength b_z using the spin-resolved data sets on Mn-Bi$_2$Se$_3$, as presented in maintext Fig. 5c.

We start from the simplest $k \cdot p$ hamiltonian for the topological surface states under TR breaking:

$$\mathrm{H} = v(k_x \sigma_y - k_y \sigma_x) + b_z \sigma_z + o(k^2) = \begin{pmatrix} b_z & vk_+ \\ vk_- & -b_z \end{pmatrix} + o(k^2) \qquad (\mathrm{S1})$$

where b_z is the magnetic interaction strength, k_+ and k_- are defined as $k_+ = k_y + ik_x$ and $k_- = k_y - ik_x$ respectively. The higher k orders $o(k^2)$ correspond to the parabolic bending of the linear dispersion at large momentum (k^2 term) and Fermi surface warping also at large momentum (k^3 term), which are not significant for surface states
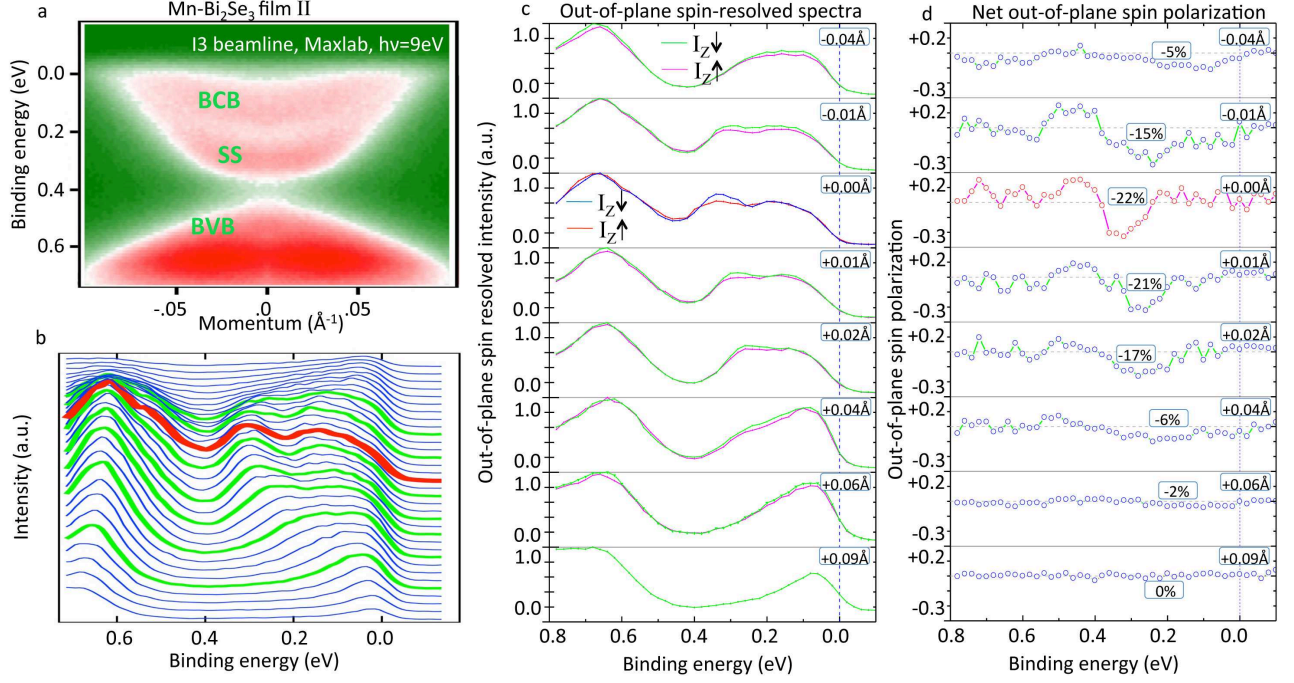
7

FIG. S5: **Out-of-plane spin measurements of Mn-Bi$_2$Se$_3$ film II. In-plane spin mea-**
surements of Mn-Bi$_2$Se$_3$ film II a-b, Spin-integrated ARPES measured dispersion and EDCs
with incident photon energy 9 eV (used for spin-resolved measurements). The EDCs selected for
spin-resolved measurements are highlighted in green (red) colors in the EDC panel. The EDC at
the $\bar{\Gamma}$ momenta is in red color. **c,** Out-of-plane spin-resolved EDC spectra. **d,** Out-of-plane spin
polarization obtained from **c.**

at the energy near the Dirac point. This description is in particularly appropriate for
Bi$_2$Se$_3$ since the surface Dirac cone is nearly isotropic and the warping effect is not
strong as comparing to Bi$_2$Te$_3$. We solve the Schrödinger equation

$$H|\psi> = E|\psi> \tag{S2}$$

The eigen-values of the energy spectrum are

$$E_{\pm} = \pm\sqrt{(vk)^2 + (b_z)^2} \tag{S3}$$

which represent the upper (E$_+$) and the lower (E$_-$) Dirac bands respectively. The
eigen-states wavefunction for upper ($|\psi_+>$) and lower ($|\psi_->$) Dirac bands are
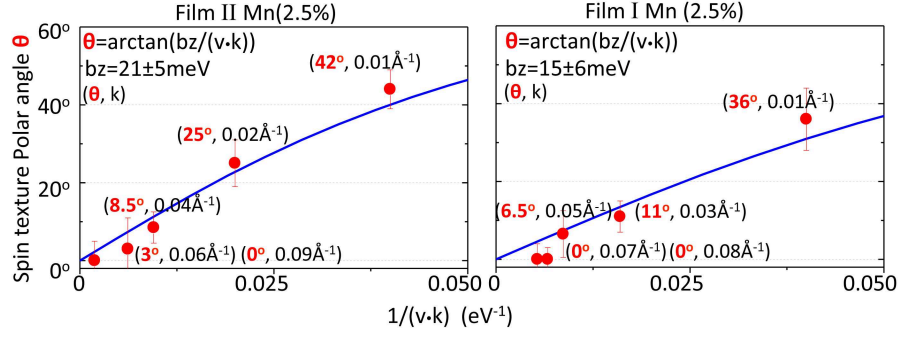
8

FIG. S6: **Surface magnetic interaction strength b_z based on spin-resolved measurements.** The magnetic interaction strength can be fitted based on the spin-resolved measurements on films II and I (see maintext Fig. 3) of Mn(2.5%)-Bi$_2$Se$_3$.

$$|\psi_+ >= \frac{1}{\sqrt{2}}e^{i\phi/2}cos(\theta/2)|\frac{1}{2} > +e^{-i\phi/2}sin(\theta/2)|-\frac{1}{2} > \quad (S4)$$

$$|\psi_- >= \frac{1}{\sqrt{2}}e^{i\phi/2}cos(\theta/2)|\frac{1}{2} > -e^{-i\phi/2}sin(\theta/2)|-\frac{1}{2} > \quad (S5)$$

where $|\pm\frac{1}{2} >$ are the eigen-states of electron spin in $\hat{z}$ direction, and (θ, ϕ) is parameterized as

$$(vk_x, vk_y, b_z) = \sqrt{(vk)^2 + (b_z)^2}(cos(\theta)cos(\phi), cos(\theta)sin(\phi), sin(\theta)) \quad (S6)$$

The angles (θ, ϕ) exactly depict the spin texture, which are measured by spin-resolved ARPES. Where θ is the out-of-plane polar angle of the spin vector, and ϕ is the in-plane azimuthal angle of the spin vector. From equation (S6), we obtain that

$$\theta = arctan(\frac{b_z}{vk}) \quad (S7)$$

This equation (S7) reflects the competition between TR-breaking effect and spin helical texture. We can use equation (S7) to fit the magnetic interaction strength b_z as presented in Fig. 5c of maintext.

As shown in Fig. S6, we have the fitting of b_z using spin-resolved date sets from films II and I of Mn(2.5%)-Bi$_2$Se$_3$ respectively. The spin-resolved data on films I and II of

9

Mn(2.5%)-Bi$_2$Se$_3$ are systematically presented in Fig. 3 of maintext, Fig. S3, Fig. S4, and Fig. S5 in the supplementary. For each measured spin vector, both in-plane spin polarization P$_{//}$ and out-of-plane spin polarization P$_z$ are measured. The spin vector out-of-plane polar angle θ is then experimentally obtained as $tan\theta = \frac{P_z}{P_{//}}$. Thus for each experimentally measured spin vector, the data can be presented in the way of (θ, k), where θ is the experimentally measured out-of-plane polar angle θ, and k is the momentum location of that spin vector in the momentum space. Using these data sets, the magnetic interaction strength b_z can be fitted by equation (S7).

Fig. S6 shows the fitting based on spin-resolved date sets from films II and I of Mn(2.5%)-Bi$_2$Se$_3$ respectively. The fitted b_z value is found to be 21 ± 5 meV for data sets fitting from film II, and 15 ± 6 meV for data sets fitting from film I.

3. **Remanent magnetization and temperature dependence of the TR breaking out-of-plane spin texture**
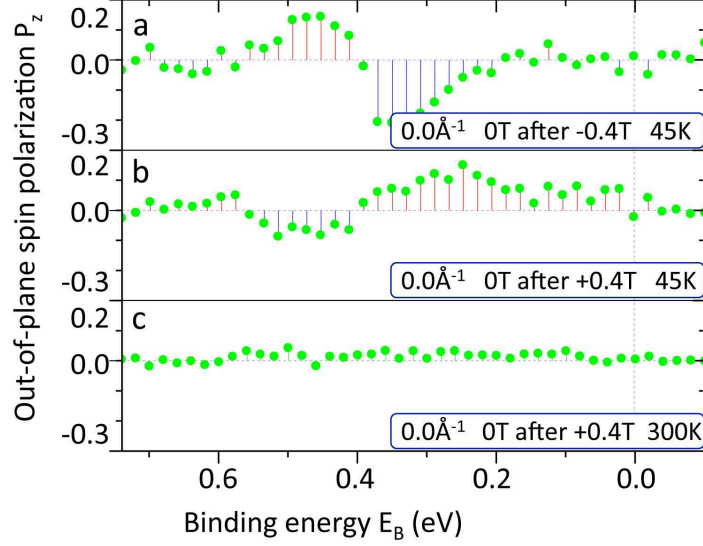

FIG. S7: **Remanent magnetization and temperature dependence of the out-of-plane spin polarization of Mn-Bi$_2$Se$_3$ film surface. a,** Out-of-plane spin polarization P$_z$ with film magnetization in -z direction at T=45 K. Such condition is achieved by apply 0.4T magnetic field in -z direction in the prep chamber and then transfer the film into the measurement chamber. **b,** Out-of-plane spin polarization P$_z$ with film magnetization in +z direction at T=45 K. Such condition is achieved by apply 0.4T magnetic field in +z direction in the prep chamber and then transfer the film into the measurement chamber. **c,** Out-of-plane spin polarization P$_z$ at T=300 K. No magnetization is induced because temperature is above Curie temperature of the film surface (see below ferromagnetic order section).

The spin-resolved data on Mn-Bi$_2$Se$_3$ shown in the main paper is done in remanent magnetization mode: the film is pre-magnetized in the UHV preparation chamber in the ARPES system at the base temperature by approaching the film with a permanent magnet with magnetic field roughly at 0.4T, in order to induce the remanent magnetization. The the film is transferred from the preparation chamber to the measurement chamber to perform spin-resolved measurements, maintaining the pressure and temperature.

Here we show the spin resolved measurements on Mn-Bi$_2$Se$_3$ film II as a function of

remanent magnetization directions and temperatures. The helical in-plane component of the spin polarization does not show any dependence with magnetization or temperature. Thus we focus on the out-of-plane component which is a direct consequence of the magnetization of the film surface. To capture the essence, we only show the out-of-plane spin polarization measurements at the TR breaking invariant $\bar{\Gamma}$ momenta $k = 0.0$ Å^{-1}. Fig. S7a repeats the measurements shown in the maintext and in Fig. S5d. When the remanent magnetization is reversed, as shown in Fig. S7b, the out-of-plane spin polarization is also observed to be reversed. Identical measurements at room temperature 300 K (Fig. S7c) show no observable out-of-plane spin polarization.

4. **First principles electronic structure calculation of Mn-Bi$_2$Se$_3$ and Mn impurity band**
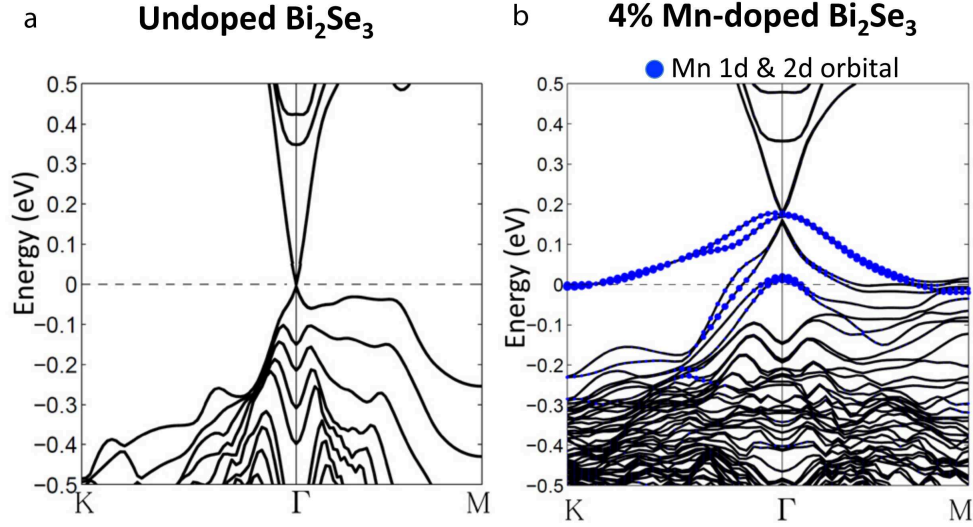

a **Undoped Bi$_2$Se$_3$** b **4% Mn-doped Bi$_2$Se$_3$**

● Mn 1d & 2d orbital

FIG. S8: **First principles electronic structures calculation of undoped and Mn-doped Bi$_2$Se$_3$. a,** undoped Bi$_2$Se$_3$. **b** 4% Mn-doped Bi$_2$Se$_3$. The band character of Mn 1d and 2d orbital are plotted on the band structure calculation.

Here we show our first principles electronic structure calculation of the Mn-doped Bi$_2$Se$_3$. Fig. S8 shows calculated band structure of both undoped and 4% Mn-doped Bi$_2$Se$_3$. Comparing to the undoped material, Mn doping is found to hole-dope the system, which moves the Fermi level (energy=0) below the Dirac point. The hole doping is due to the 2^+ ionic state for Mn atom (as compared to a 3^+ ionic state for the Bi atoms in Bi$_2$Se$_3$). Such p-type doing behavior is also directly observed in our ARPES measurements.

Apart from moving the chemical potential, an important feature in the calculation is the development of extra electronic states with strong Mn orbital character (Mn impurity bands). The impurity bands are observed to be majorly located at energies lower than 0.3 eV below the Dirac poin in our calculation (see Fig. S8b). At the same time, the valence band spectral weight is found to be shifted from $k_{//} \simeq \pm 0.1$ Å^{-1} to $k_{//} \simeq 0.0$ Å^{-1} by Mn doping, as shown in Fig. 1c in the maintext, measured with the same photon energy. The newly developed strong intensity at the valence band of

13

Mn-Bi$_2$Se$_3$ in ARPES measurements can have strong correlations to the Mn impurity bands in the calculation.

5. Ferromagnetic ordering in Mn-Bi$_2$Se$_3$ film
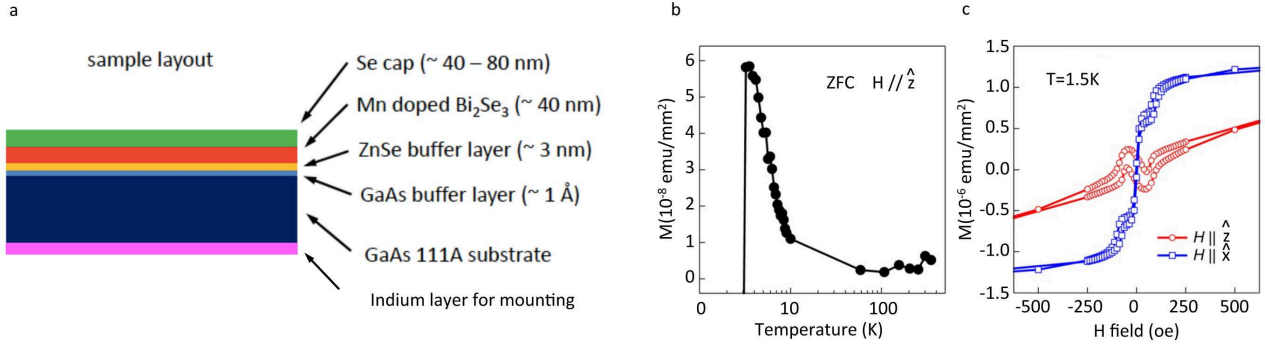
5.1. SQUID measurements of Mn-Bi$_2$Se$_3$ film

FIG. S9: **Magnetic property of Mn-Bi$_2$Se$_3$ measured by SQUID. a,** Mn-Bi$_2$Se$_3$ film sample layout. The indium layer on the bottom which is necessary for the sample mounting for MBE growth becomes superconducting below 4 K which contributes a very large diamagnetic signal to the SQUID measurements . **b,** Remanent magnetization measurements of Mn-Bi$_2$Se$_3$ film with zero field cooling (ZFC). The big drop of magnetization signal comes from the indium layer at the back side of the sample. **c,** Hysteresis measurements at T=1.5 K. The anomaly at H $\sim$ 0 again comes from the diamagnetic signal of the superconducting indium layer on the back side of the sample.

As a starting point, the magnetic property of the Mn-Bi$_2$Se$_3$ film can be measured by superconducting quantum interference device (SQUID). As shown by the remanent magnetization measurements on the samples in Fig. S9b, clear remanent signal can be observed for temperatures below 10 K. Clear hysteresis is also shown by SQUID below 5 K (Fig. S9c). The anomalous drop of the magnetization signal in both remanence and hysteresis comes from the diamagnetic signal of the superconducting indium layer (below 4 K) on the back of the film sample, which is not relevant to the magnetic property of the Mn-Bi$_2$Se$_3$ film itself at all.

In general, SQUID measurements are not so sensitive to small magnetization signals. In fact, small remanent signal is observed by SQUID above 10 K, but the signal is

14

too small and no clear hysteresis is observed as a result. Moreover, SQUID includes magnetization signal of the entire sample (even the irrelevant indium superconducting diamagnetic signal on the back side of the sample). Thus a surface sensitive magnetometer with a better sensitivity to small magnetization signal is needed to measure the magnetic properties on the top surface of the Mn-Bi$_2$Se$_3$ film, where the topological surface electrons are localized, as well as where ARPES and spin-resolved ARPES mainly probe (within ~ 20 Å).

5.2. XMCD measurements on the top surface of the Mn-Bi$_2$Se$_3$ film

The magnetic properties of the surface of the Mn-Bi$_2$Se$_3$ film need to be treated carefully for two reasons: (i) It has been theoretically predicted that the ferromagnetic order of the TI surface can be achieved via the Ruderman-Kittel-Kasuya-Yosida (RKKY) interaction mediated through the topological surface Dirac fermions [10], even in absence of the bulk magnetic ordering [11]. (ii) More importantly, careful Mn concentration characterization measurements have found that the surface has much higher Mn concentration than the entire film crystal [12]. The Mn concentration of the entire film crystal, which is the nominal concentration used in the maintext, is measured by the in-situ Bi/Mn flux ratio during the MBE growth in conjunction with ex-situ Rutherford back scattering, both of which reveal the ratio of Mn atoms versus the Bi atoms over the entire crystal. On the other hand, the depth profile of Mn doping concentration can be measured by secondary ion mass spectrometry (SIMS), which shows that an excess of Mn accumulates on the surface during the sample growth. SIMS shows that for the top 50 Å of the surface, the Mn concentration is about 8 times higher than deep in the bulk. Finally, scanning tunneling microscopy (STM), which solely probes the top surface, also reveals a much higher Mn concentration on the surface as compared to the nominal Mn concentration, as well as the the fact that Mn atoms are inhomogeneously distributed on the surface, including the presence of clusters of Mn atoms on the sample surface [12]. The high Mn concentration on the surface is very likely to be due to the diffusion of Mn atoms toward the film surface at high temperatures (> 200 K) during MBE growth or during decapping procedure used for ARPES and STM measurements. In the well-known dilute magnetic semiconductors (Ga, Mn)As, the Curie temperature is found to be proportional to the Mn

concentration. Mean-field Zener model [13] predicts $T_c \propto x \cdot p^{1/3}$, where x is the doping concentration of Mn to Ga, and p is the hole carrier density. Therefore the high Mn concentration on Bi_2Se_3 film surface and its p-type doping to the Bi_2Se_3 system are both favorable to the ferromagnetic order on the surface at the relatively high temperatures(> 10 K).

Here we use the total electron yield (TEY) mode of X-ray magnetic circular dichroism (XMCD, for review of the technique and its application to transition metal thin films and monolayers, see [14, 15]) to directly measure the magnetization of the surface.

5.2.1. X-ray absorption and total electron yield mode

X-ray magnetic circular dichroism (XMCD) is based on the X-ray Absorption Spectroscopy (XAS), which is a technique used to probe the electronic configuration of a specific element within a material. Scanning the photon energy over the chosen element's absorption edge results in a sharp increase in the x-ray absorption. Electrons from an initial core state are promoted to the lowest unfilled state with allowed symmetry, just above the Fermi level. After absorption, the atom relaxes by two channels simontaneously. In the Auger process, an intermediate electron recombines with the core hole and the energy of the excitation is carried away by the ejection of a secondary electron, which can be detected by total electron yield (TEY) signal from the sample surface. The other channel is fluorescent photon emission, the inverse of the absorption process, where the excited electron recombines with the core hole and emits a photon, which can be measured by the fluorescence yield using a photodiode. Here we choose the TEY mode of the XMCD. The surface sensitivity is then basically the surface electron mean free path, at the range of $\sim 30 - 50$ Å, which is suitable for our purpose. The TEY mode of the XMCD has been used to measure ferromagnetic properties of various transition metals or dilute magnetic semiconductors in thin films or nanostructures in the past [15–17].

XAS and XMCD measurements are performed at the back-endstation of D1011 beamline at Maxlab in Lund, Sweden, with TEY mode. Fig. S10a shows the measured XAS intensity of the Mn L-edge on the top surface of the Mn-Bi_2Se_3 film, the same batch as used for spin-resolved measurements in the maintext (nominal concentration Mn=2.5%). The sample is prepared the same way as in the ARPES measurements
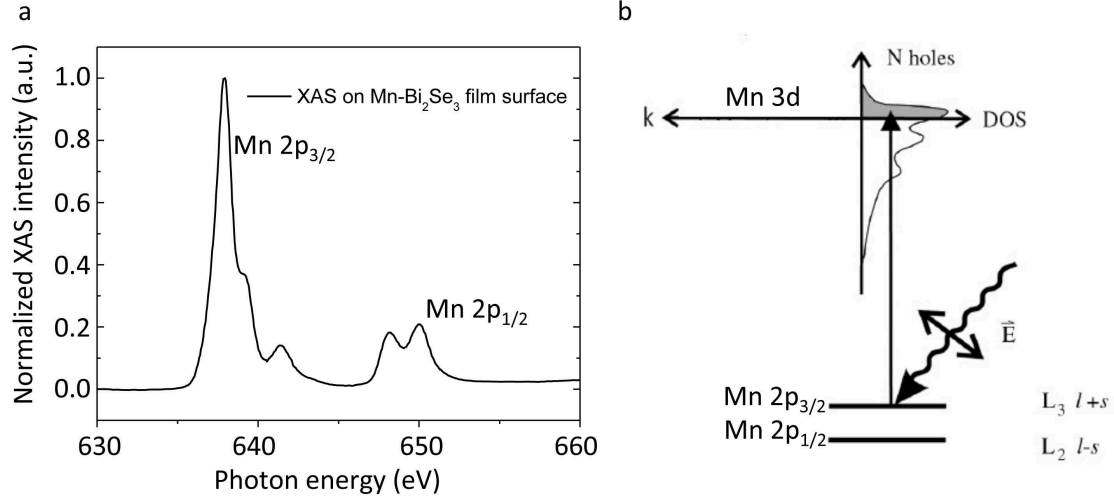
FIG. S10: **XAS of Mn L-edge on the top surface of Mn-Bi$_2$Se$_3$ film. a,** Normalized XAS intensity of Mn L-edge on the top surface of Mn-Bi$_2$Se$_3$ film. The nominal Mn concentration of the entire crystal is Mn=2.5%. **b,** Schematic illustration of photon excitation of Mn L-absorption edge.

in situ by decapping inside the XMCD UHV chamber for consistency. The lineshape of the observed Mn L-edge here is typical for Mn^{2+} ionic state such as in (Ga,Mn)As dilute magnetic semiconductor [16], which indirectly proves the p-type doping of Mn atoms in Mn-Bi$_2$Se$_3$ film.

5.2.2. XMCD principle review

the origin of the XMCD effect can be explained by a simple two step model which may be visualized by means of Fig. S11. Here we have arbitrarily assumed that the magnetization is in the down direction, defined as the -z axis of a Cartesian coordinate system. If the wavevector $\vec{k}$ of the X-rays is aligned along the +z axis, the photon spin is up with a value $+\hbar$ (down with a value $-\hbar$) for right (left) circularly polarized X-rays. In the first step, right or left circularly polarized photons transfer their angular momentum, $+\hbar$ and $-\hbar$, respectively, to the excited photoelectron. The electron carries the angular momentum either by the spin or the orbital degree of freedom. Because the spin does not interact directly with the electric field, in the absence of spin-orbit coupling, one can only transfer the photon angular momentum to the orbital part. This is the case for the excitation from an atomic s core-state or if one sums over
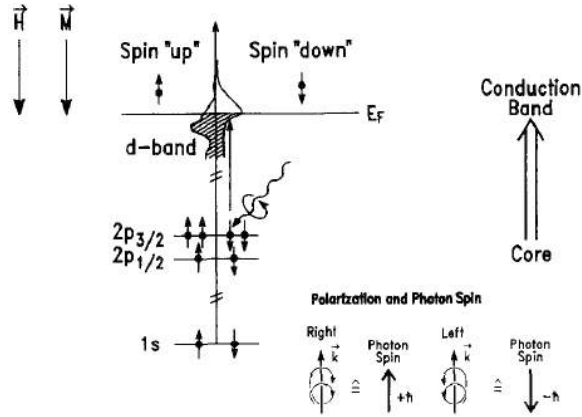
17

FIG. S11: **Electronic transitions in XMCD illustrated in a one-electron model. Adapted from Ref. [14]** The transitions occur from a core shell (typically L shell) to empty conduction band states above the Fermi level, labeled E_F. The band occupation is shown here for an external magnetic field in the "down" direction. i.e. $\vec{H}//-z$. Also shown is the correlation of the helicity and wavevector $\vec{k}$ for right and left circular polarization and the photon spin directions. If the light is incident in the +z direction. the photon spin for right circularly polarized light is "up" and has the value $+\hbar$. The dichroism intensity is defined as the difference between a spectrum obtained with antiparallel relative orientation of photon spin and external field direction and a spectrum with parallel relative orientation.

both spin-orbit components (L_3 plus L_2) of a p core-state. If the core-state is split by the spin-orbit interaction (like Fig. S10a), the substates are no longer pure spin states. As a result, the photon angular momentum is transferred to both the orbital and spin degrees of freedom of the excited photoelectron. In fact, a relatively large portion can be transferred to the spin resulting in spin polarized photoelectrons. For the $p_{3/2}$ initial state (L_3 edge), for example, $\vec{l}$ and $\vec{s}$ are parallel, and therefore, transfer of the angular momentum $+\hbar$ by right circularly polarized light excites more (62.5%) spin-up than (37.5%) spin-down electrons. The reverse holds for left circularly-polarized light. For the $p_{1/2}$ initial state (L_2 edge) $\vec{l}$ and $\vec{s}$ are anti-parallel and right circularly polarized light preferentially couples to spin-down electrons (75% spin-down and 25% spin-up electrons). Again, left circularly polarized light does the opposite. Note, that in the first step spin-up and spin-down are defined relative to the photon spin direction,

18

and the discussed effects are therefore independent of the magnetic properties of the sample.

The magnetic properties enter in the second step. Here the valence shell acts as a detector for the spin and/or orbital momentum of the excited photoelectron. The quantization axis of the detector is given by the which needs to be aligned with the photon spin direction for maximum dichroism effect. If the metal is ferromagnetic, an imbalance in empty spin-up and spin-down states will exist and hence, the valence shell can act as a spin detector. Similarly, the valence shell will act as an orbital momentum detector if there is an imbalance of states with different magnetic quantum numbers m_{l}. i.e. in case of spin-orbit splitting in the valence shell. Therefore, for K-shell excitation or for summed L_3 and L_2 spectra, a dichroism effect exists only if the valence shell exhibits an orbital moment. By separating the L_3 and L_2 components one becomes sensitive to the spin. Sum rules allow one to quantitatively separate the spin and orbital magnetic contributions of the valence shell in the electronic ground state.

5.2.3. XMCD on Mn-Bi$_2$Se$_3$ film top surface at T=45 K

Fig. S12 shows the XMCD measurements on Mn-Bi$_2$Se$_3$ film top surface. The remanent measurements are performed at T=45 K and H=0T after applying magnetic field H=0.5T along -z direction (see Fig. S11). If the surface is ferromagnetically ordered at 45 K, then a finite remanent magnetization $\vec{M}$ should take place along -z direction after applying the magnetic field. Such remanent magnetization then will lead to a different response of the XAS spectrum using circular plus or circular minus polarized light, resulting in a nonzero remanent XMCD. Indeed, a clear difference between the different photon spin XAS spectra are observed, as shown in Fig. S12a. The L_3 edge is observed to be enhanced with photon spin parallel to the magnetization, whereas the L_2 edge is enhanced with photon spin anti-parallel to the remanent magnetization. The clear remanent XMCD (Fig. S12b) suggests that the surface is ordered with easy axis along the out-of-plane direction at T=45 K.

The hysteresis then can be measured by measuring XMCD signal (we choose the peak energy ofs L_3 edge E~638.2 eV) at different applied H fields. As shown in Fig. S12c, a clear hysteresis is observed at T=45 K along out-of-plane direction, which proves the
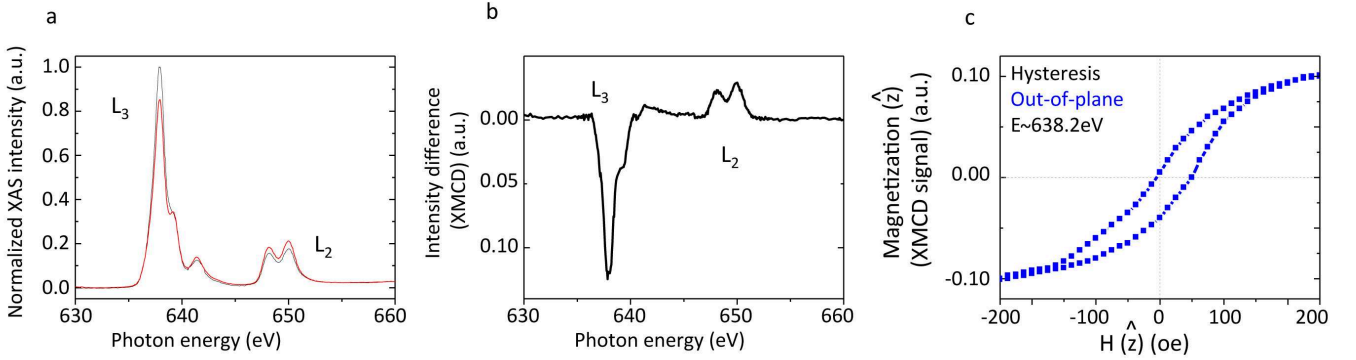
FIG. S12: **XMCD measurements at Mn L_{23} absorption edge on Mn-Bi$_2$Se$_3$ film top surface at T=45 K. a,** Remanent normalized XAS intensity of Mn L_{23} absorption edge. Black (red) represents the XAS with the photon spin parallel (anti-parallel) with the remanent magnetization. **b,** The difference of the two XAS (parallel and anti-parallel) generates the XMCD signal, which is proportional to the magnetization of the Mn-Bi$_2$Se$_3$ film top surface. **c,** Hysteresis measurements are performed with field applied along out-of-plane direction. The measurements are done by measuring XMCD signal at the L_3 edge energy E∼638.2 eV at different H fields.

ferromagnetic order of the Mn-Bi$_2$Se$_3$ film top surface.

5.2.4. XMCD temperature dependence

Fig. S13 shows the temperature dependence of the XMCD signal. The XMCD signal is proportional to the remanent magnetization of the film surface, which can be obtained by the sum rules [18] (see below). Thus, the temperature dependence of the remanent XMCD signal reveals the temperature dependence of the magnetic ordering of the film surface. As shown in Fig. S13, clear XMCD is observed at T=45 K, whereas the XMCD is strongly suppressed at T=110 K. Finally no XMCD is observed from the measurement performed at room temperature. The detailed Curie temperature of the surface requires future finer measurements with more intermediate temperatures.

5.2.5. Sum rules and magnetic moment per Mn atom

Finally, we apply the sum rules to the experimentally measured XMCD spectra to obtain the magnetization of the Mn-Bi$_2$Se$_3$ film top surface. From Fig. S12a-b, we
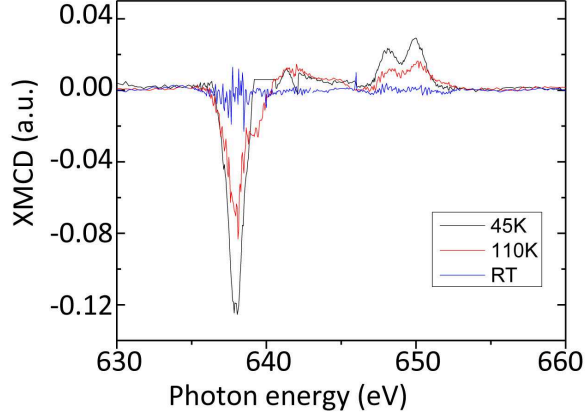
20

FIG. S13: **Temperature dependence of remanent XMCD.** XMCD measurements are performed at three different temperatures: T=45 K, 110 K and 300 K (room temperature).

have:

$$I_{\text{total}} = I_{\text{para}} + I_{\text{anti-para}} \tag{S8}$$

$$I_{\text{XMCD}} = I_{\text{anti-para}} - I_{\text{para}} \tag{S9}$$

where I_{para} and $I_{\text{anti-para}}$ are the two XAS spectra with photon spin parallel or anti-paralel to the magnetization shown in Fig. S12a. I_{total} is the sum of the two XAS spectra. I_{XMCD} is the XMCD signal which is the difference between the two XAS spectra shown in Fig. S12b. Then according to the well-established sum rules [18], the spin magnetic moment in the unit of μ_{B}/Mn atom is:

$$m_{\text{spin}} = -\frac{6\int_{\text{L}_3} I_{\text{XMCD}}\, d\text{E} - 4\int_{\text{L}_3+\text{L}_2} I_{\text{XMCD}}\, d\text{E}}{4\int_{\text{L}_3+\text{L}_2} I_{total}\, d\text{E}} \times (10 - n_{3d})(1 + \frac{7 < \text{T}_z >}{2 < \text{S}_z >})^{-1} \tag{S10}$$

where n_{3d} is the $3d$ electron occupation number of Mn atom. The L_3 and L_2 denote the integration range. $< \text{T}_z >$ is the expectation value of the magnetic dipole operator and $< \text{S}_z >$ is equal to half of m_{spin} in Hartree atom units. For Mn, as a starting point, we neglect the d^{5+}hole complex [19], use $n_{3d} = 5$ and $< \text{T}_z > \sim 0$. Using the XMCD at T=45 K in Fig. S12b, we obtain an average spin magnetic moment of $1.3\mu_{\text{B}}$ per Mn atom.

21

SI III. Gap-like feature at the Dirac point in nonmagnetic TI materials and special Dirac point nature

Experimentally, although some forms of magnetism in TI material have been reported by bulk doping [20, 21] or surface deposition doping [22], the concrete signature of TR symmetry breaking of topological surfaces is far lacking. The simplest physical scenario used in all theoretical proposals [23–26] is that of an energy gap opened at the TR invariant momenta or the Kramers' point via ferromagnetism. Consequently, a number of experiments have been performed to address the electronic states (without spin sensitivity) near the Dirac point of TIs with bulk magnetic dopants or under surface magnetic deposition [11, 27, 28]. Although suppression of photoemission measured density of states at the Dirac point has been reported and presumed as the magnetic gap [11, 27, 29], a number of other factors, such as spatial fluctuation of momentum and energy near the Dirac point [30] and surface chemical modifications [27] possible in the samples challenge the gap to be of magnetic origin [30, 31]. The experimental probes previously used to address the gap cannot distinguish or isolate these factors that respect TR symmetry from the TR breaking effect as highlighted in most recent STM works, for example by Beidenkopf *et al* [30]. In fact, "gap"-like feature is also observed even on a number of nonmangetic TI systems (see below). These gaps can appear due to ad-atom hybridization, surface top layer relaxation, Coulomb interaction from deposited atoms, spatial fluctuation of surface electronic potential and other forms of surface chemistry such as in situ oxidation [27, 30, 32]. Upon until now, it has not been not possible to isolate TR breaking effect from the rest of the extrinsic surface gap phenomena reported in various experiments [27, 30, 32]

Here we thoroughly discuss the "gap" (photoemission intensity dip) observed at the Dirac point in spin-integrated ARPES, and illustrate the difficulty to use it as a concrete evidence of TR breaking effect in TI.

1. **Gap-like feature observed in spin-integrated ARPES**

   We start by showing high-resolution spin-integrated ARPES measured dispersion on various TI compounds, focusing on the Dirac point regime. All the samples in this section are bulk single crystals whose surface for ARPES measurements is prepared by *in situ* cleavage. The stoichiometric compound without sulfur substitution $TlBiSe_2$ Cleave I, II, and III (Fig. S14a-c) are different pieces of crystals from the same growth
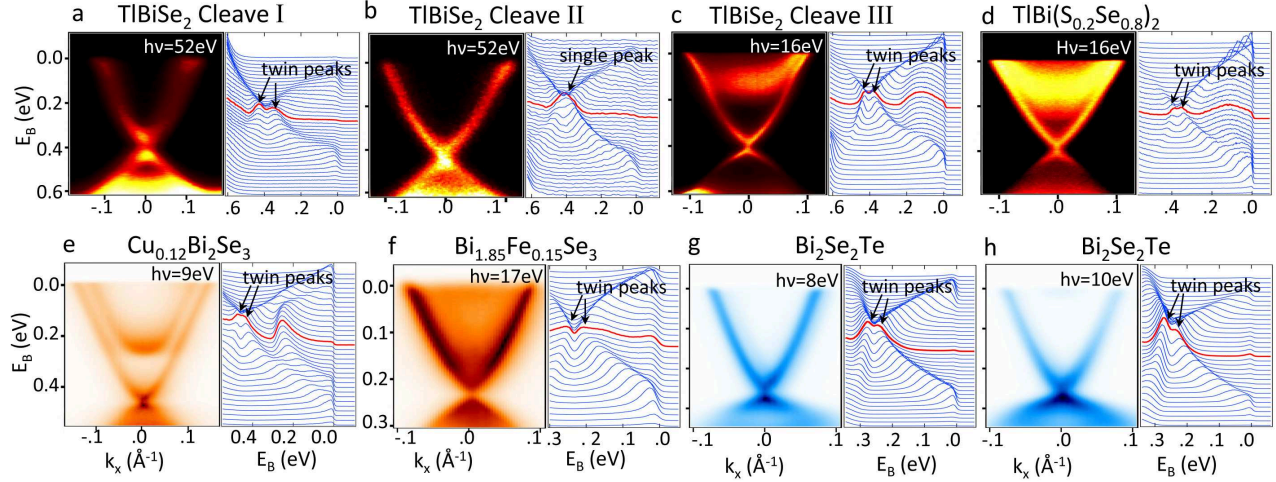
FIG. S14: **Electronic states at the Dirac point region for various topological insulator compounds.** High-resolution ARPES and energy distribution curves (EDCs) highlighting the Dirac point region of different compounds. Incident photon energy (hν) used for the measurement is noted. The TlBiSe$_2$ Cleave I, II, and III (**a-c**) are from the same growth batch but different pieces of the crystal. The two Bi$_2$Se$_2$Te panels (**g and f**) are from the same cleavage on one piece of sample, using different incident photon energies. The energy scale of the intensity dip (separation between the twin peaks) are obtained by fitting the EDC by Lorentzian peaks (same approach as Ref [11].

batch. While a clear intensity dip and a "twin peaks" behavior are observed for TlBiSe$_2$ Cleave I, Cleave II shows a very bright and intact Dirac point with "single peak" in the EDC profile. Cleave III also exhibits a "twin peaks" profile but relatively weaker than Cleave I. The system with 20% sulfur substitution TlBi(S$_{0.2}$Se$_{0.8}$)$_2$ (Fig. S14d) shows a similar weak "twin peaks" profile as TlBiSe$_2$ Cleave III. The observed Dirac point intensity dip is not only confined within the thallium-bismuth-selenium-sulfur system, but also can be seen for various Bi$_2$Se$_3$ and Bi$_2$Te$_3$ based compounds, as shown in Fig. S14e-h. The energy separation scale of the twin peaks ("gap size") is listed on each panel, which is comparable to the previous studies [11, 29].

Systematic studies are perfomed to rule out possibilities that our observations are owning to unphysical experimental errors or artifact: first, the Dirac point intensity dip is not due to photoemission matrix element effect caused by a particular photon energy. Fig. S14g-h show ARPES measurements on the same cleavage of Bi$_2$Se$_2$Te
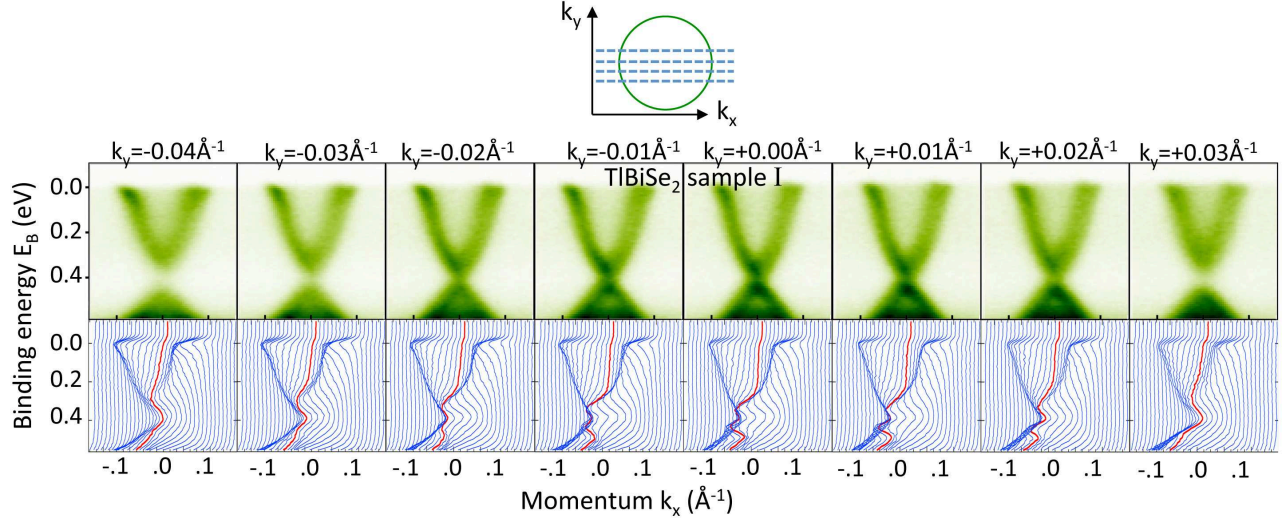
FIG. S15: **Intensity dip at the Dirac point shown by (E, k_x, k_y) mapping.** ARPES (E, k_x, k_y) mapping on TlBiSe$_2$ Cleave I (see Fig.1). Each single ARPES dispersion measurement generates a two dimensional map with energy (vertical axis) versus momentum (k_x) (horizontal axis). In order to probe the other in-plane momentum direction (k_y), the angle of the sample with respect to the electron analyzer is changed. The (E, k_x, k_y) mapping rules out the possibility of "angle misalignment" which can cause an artifact "gap" at the Dirac point.

crystal using identical experimental settings but only different photon energies. Indeed different photon energies can selectively enhance (or suppress) the intensity of certain electronic states. However, the EDC profile remains to be a "twin peak" profile though the relative intensity between the two peaks can vary at different photon energies. Moreover, a parallel evidence is that TlBiSe$_2$ Cleave I and II are using identical experimental settings (including same photon energies), but just different pieces of crystal from the same batch. However, whereas Cleave I shows "twin peaks", Cleave II shows "single peak". These facts prove that the Dirac point intensity dip and "twin peaks" EDC profile are not resulted from the choice of certain photon energy. Second, the observation is also not caused by "angle misalignment" in ARPES experiment, as shown in Fig. S15. Typically, a single ARPES dispersion map generates a 2D mapping with energy (vertical axis) versus momentum k_x (horizontal axis). In order to probe the other in-plane momentum direction k_y, the angle of the sample with respect to the electron analyzer slit is changed (the out-of-plane momentum direction k_z is obtained

24

by changing incident photon energy, which is not relevant in our case because the topological surface states are 2D without k_z dispersion). Therefore, in order to measure the electronic states at the Dirac point ($k_x = k_y = 0$), one needs to position the angle of the sample so that $k_y = 0$. Here we show a series of ARPES dispersion maps with angle increment of 0.2 degree (corresponding to ~ 0.01 Å^{-1} k_y increment). It can be seen clearly that the intensity dip never goes away throughout the k_y mapping, which rules out the "angle misalignment" possibility.

For the stoichiometric or nonmagnetically doped compounds (Fig. S14a-e, g-h and Fig. S15), no global magnetic ordering is observed. The results on thallium-bismuth-selenium-sulfur system is inconsistent with the Higgs mechanism in Ref. [29], since we observe clear intensity dip on TlBiSe$_2$ Cleaves I and III. Rather, we found that whether the Dirac point intensity dip and the "twin peaks" EDC will show up is cleavage-dependent, as seen in Fig. S14a-c. Our experience shows that for nonmagnetic topological insulator single crystals, the Dirac point intensity dip occurs in roughly 5% to 10% of the cleavages. Since no microscopic level magnetization measurements (magnetization measurements with spatial resolution better than ~ 10 μm^3) are available, we cannot definitely rule out the possibility that the intensity dip at the Dirac point on these nonmagnetic compounds is caused by micro-domain magnetization owning to spontaneous symmetry breaking. However, it is very unlikely that spontaneous symmetry breaking occurs on all these nonmagnetic compounds without strong correlation, especially when considering that the observed intensity dip is cleavage dependent. In contrast, the magnetically-doped Bi$_{1.85}$Fe$_{0.15}$Se$_3$ (Fig. S14f) exhibits the Dirac point intensity dip and "twin peaks" EDC profiles for all the 10 cleavages of crystals we have measured, which demonstrates some difference between samples with or without magnetic dopants.

2. **Tentative explanations and special nature of the Dirac point**

Here we provide a few tentative explanations that can cause photoemission intensity suppression at the Dirac point without breaking TR symmetry to explain the observed "gap" in the nonmagnetic compounds above.

Firstly, since the Van der Waals bonding between the quintuple layers (QLs) of Bi$_2$Se$_3$ (or the corresponding unit cell for other layered-structure topological insulators) is
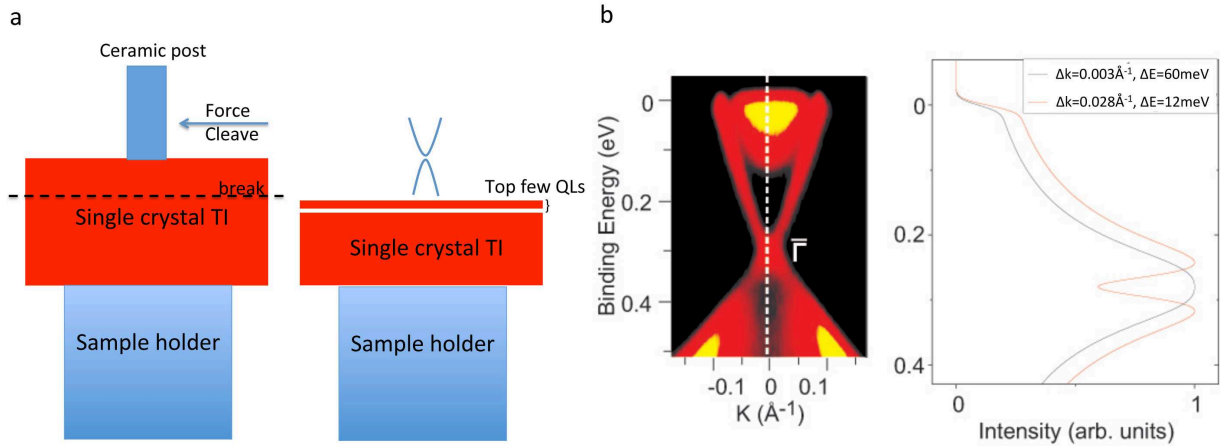
FIG. S16: **Tentative explanations of the intensity dip ("gap") at the Dirac point. a,** The top few quintuple layers (QLs) of the TI single crystal can be lifted up and relatively isolated to the rest of the crystal. The coupling between the top and bottom surfaces of the top QLs opens up a gap at the Dirac point. Such top few QLs isolation might be caused by the ARPES sample preparation (mechanical cleavage). Alternatively it might be caused by chemical intercalation due to phase separation in the crystal growth. **b,** Special nature of the Dirac singularity. Our simulation shows that substantial momentum broadening automatically leads to a "twin peak" lineshape of the density of states at the Dirac point.

weak, it is possible that the top few QLs of the sample surface can be lifted up and become relatively isolated from the rest of the crystal. In this case, a gap at the Dirac point will be opened by coupling between the top and bottom topological surface states of the ultra-thin topological insulator film. In this scenario, the ARPES intensity dip at the Dirac point represents a true gap (ideally zero density of states within the gap), but the system still respects TR symmetry because the degeneracy at the $\bar{\Gamma}$ point is not lifted up (The number of electronic states are doubled because the top and bottom surface states are degenerate). The top few QLs can be lifted up by the mechanical cleavage or exfoliation (the typical method to prepare clean surface of single crystals for ARPES measurements), which also partly explains the observed cleavage dependence. Alternatively, chemical intercalation due to phase separation in the crystal growth can have similar effect. For example, for a metal-doped Bi_2Se_3 ($M_x Bi_2 Se_3$), phase

26

separation can cause the real chemical composition to be $Bi_2Se_3 \cdot (MSe)_x$. The MSe layer (or even the single element metal layer) can intercalate in between the Bi_2Se_3 QLs, lifting the top Bi_2Se_3 layers up.

Secondly, the intrinsic nature of the Dirac point of Dirac fermions requires it to be treated with special care. Spatial inhomogeneity caused by dopants, disorders or defects is found to lead to spatial fluctuations of energy and momentum of the surface electronic states by STM [30]. The real space spatial fluctuation of momentum leads to a momentum broadening Δk in momentum space. Because the electronic states at the vicinity of the Dirac point has long wavelength (small k), a finite momentum broadening can lead to considerable modification to the density of states at small momentum when $\Delta k \sim k$. In fact, our simulation shows that a momentum broadening at the Dirac point will automatically generate a dip of the intensity (density of states) at the Dirac point (Fig. S16b) very similar to the intensity dip shown above as well as in previous reports [11, 29].

Here we explain the special nature of the Dirac point and its energy and broadening in detail: the broadening of electronic states along momentum and energy axes is a well known phenomenon that must be treated in an unusual way at Dirac singularities. Energy broadening occurs because energy and time are conjugate variables, and the finite lifetime of electronic states due to scattering causes their width along the energy axis to be non-zero. By the same token, momentum (e.g. 'k_x') and spatial variables (e.g. 'x') are conjugate to one another, and states are broadened along the momentum axes because scattering and localization restrict the translational symmetry of single-particle electronic states. For a band with small curvature, energy and momentum broadening cannot be readily distinguished and it is sufficient to broaden only in energy in comparing between theoretical band structure calculations and data. Dirac point singularities are a special case for which energy and momentum broadening cause distinctly recognizable effects [33]. As an example, it is well known that the momentum-integrated electronic density of states goes to zero at a Dirac point in the absence of the self energy broadening. Momentum broadening does not affect the distribution of electronic states along the energy axis, and thus allows the density of states at the Dirac point to remain zero. Energy-axis broadening (imaginary self

27

energy) causes the momentum-integrated density of states at the Dirac point energy to become non-zero and to approach the Dirac point energy in a parabolic rather than linear fashion.

This contrast can be seen immediately in the ARPES EDC (constant momentum) curves plotted in Fig. S16b. ARPES intensity at the $\overline{\Gamma}$ point is roughly proportional to the total momentum-integrated density of states so long as the Dirac band momentum is much smaller than the intrinsic momentum width, meaning that the ARPES intensity falls to nearly 0 at the Dirac point binding energy for the Bi_2Se_3 Dirac cone. Accounting for this effect at a Dirac point requires that the intrinsic momentum and energy widths be treated separately, a procedure usually neglected for non-Dirac bands that contain no sharp kink or singularity. As an example of how such a fit can be conducted, we have chosen two sets of momentum and energy broadening parameters (Lorentzian Δk=0.0275 Å^{-1}, 0.003 Å^{-1} and ΔE=12 meV, 60 meV) representing cases in which momentum broadening dominates and energy broadening dominates, respectively. The fitted lineshape is then obtained by broadening an ideal Dirac cone with velocity v_D=2.3 eV-Å through Lorentzian convolution in momentum and energy (convoluting each point $[k_{x0}, k_{y0}, E_0]$ with $I \propto \frac{1}{(k_x-k_{x0})^2+(k_y-k_{y0})^2+(\Delta_k/2)^2} \times \frac{1}{(E-E_0)^2+(\Delta_E/2)^2}$). As shown in Fig. S16b, with substantial momentum broadening (Lorentzian Δk=0.0275 Å^{-1}, ΔE=12 meV), the simulated EDC profile is found to develop an intensity dip at the Dirac point. The "twin peak" lineshape shows great resemblance to the spectra weight suppression reported by ARPES experiments [11, 29]. However, we would like to emphasize that the above simulated intensity dip arises purely from momentum broadening near the Dirac singularity, which is not related to any TR breaking effect.

Apart from the above factors, impurity bands near the Dirac point originated from dopants or chemical substitutions can also take place in the above single crystals and samples in previous reports [11, 29]. The coexistence (degeneracy) of the topological surface states with the impurity bands can change the well-defined surface electronic states into finite lifetime surface resonance, which can possibly suppress the ARPES measured intensity of the surface states. All these possibilities contribute complexity to the intensity dip at the Dirac point from spin-integrated ARPES. However, they all respect TR symmetry and can be ruled out with a spin-sensitive experimental probe. Since the spin-integrated ARPES

is not spin-sensitive and cannot test the Kramers degeneracy theorem directly like how we demonstrated in the maintext, using such intensity dip as the TR breaking evidence can be risky.

SI IV. Zn-Bi$_2$Se$_3$

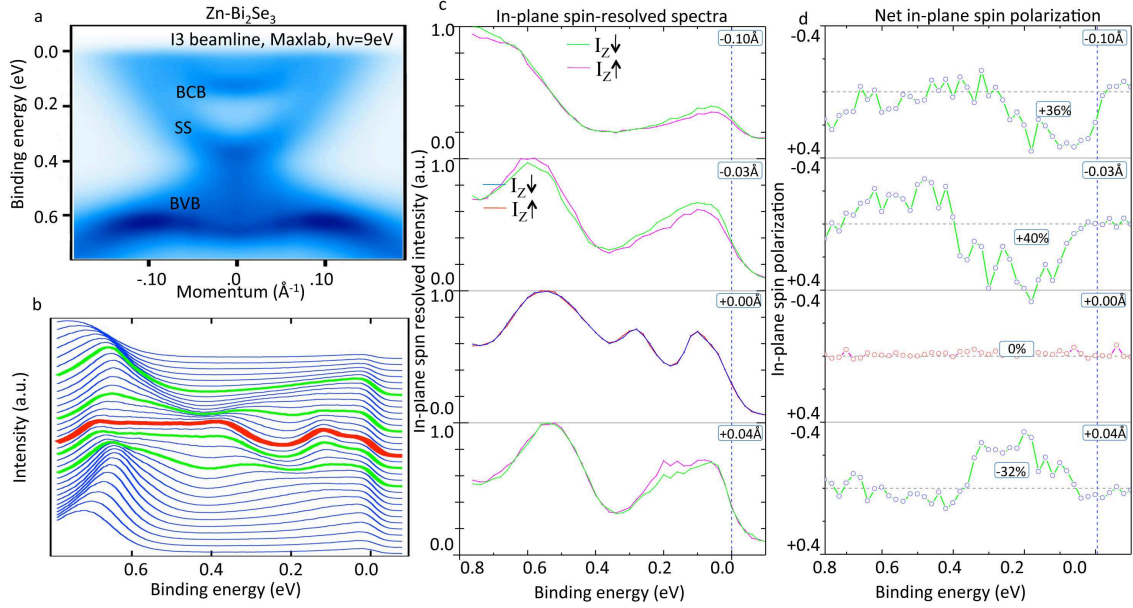## 1. Detailed spin-resolved measurements on Zn-Bi$_2$Se$_3$

FIG. S17: **In-plane spin measurements of Zn-Bi$_2$Se$_3$. a-b,** Spin-integrated ARPES measured dispersion and EDCs with incident photon energy 9 eV (used for spin-resolved measurements). The EDCs selected for spin-resolved measurements are highlighted in green (red) colors in the EDC panel. The EDC at the $\bar{\Gamma}$ momenta is in red color. **c,** In-plane spin-resolved EDC spectra. **d,** In-plane spin polarization obtained from **c**.

Here we show comprehensive spin-resolved measurements on Zn-Bi$_2$Se$_3$. These measurements on Zn-Bi$_2$Se$_3$ are performed at the I3 beamline at Maxlab [1, 2] in Lund, Sweden, with incident photon energy 9 eV as a control group to the Mn-Bi$_2$Se$_3$. For in-plane spin polarization (see Fig. S17), the spin-helical configuration is again observed without surprise. On the other hand, the out-of-plane spin polarization (see Fig. S18) is zero at small momentum near the $\bar{\Gamma}$ momenta which is in sharp contrast to the Mn-Bi$_2$Se$_3$ case. At large momentum ($k \sim -0.10$ Å) a very small but finite P$_z$ appears. However, the P$_z$ in Zn-Bi$_2$Se$_3$ respects TR symmetry since it reverses its sign upon going from $-k$ to $+k$. As shown by Fig. S18b, the Fermi surface of Zn-Bi$_2$Se$_3$ is warped into hexagon-shape. Therefore, the observed P$_z$ should be a result of the Fermi surface warping on the Zn-Bi$_2$Se$_3$ Dirac cone [34].
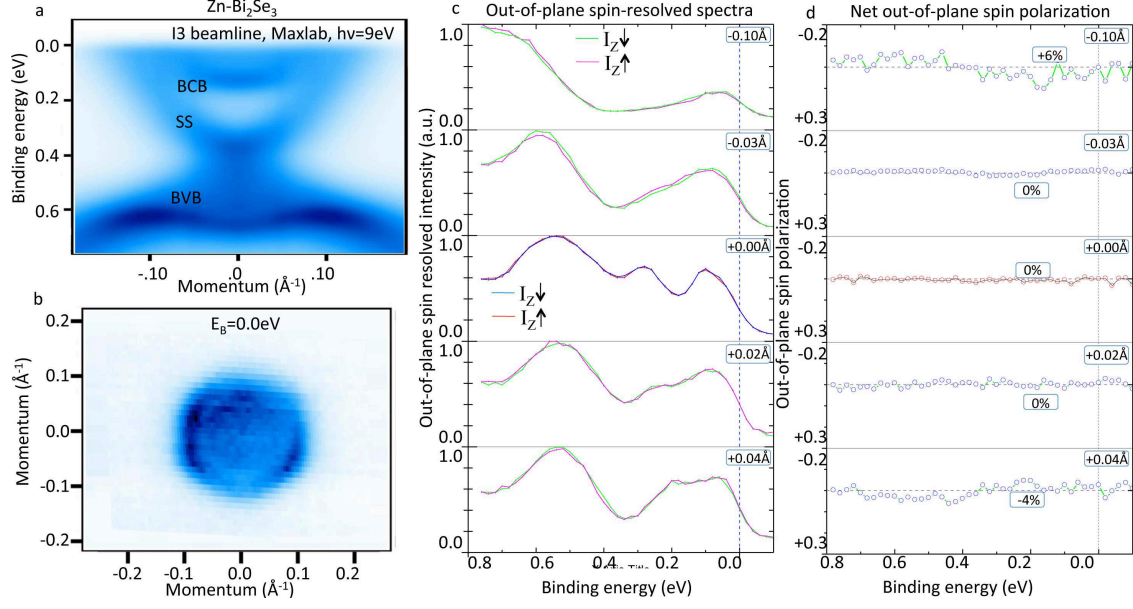
FIG. S18: **Out-of-plane spin measurements of Zn-Bi$_2$Se$_3$. a,** Spin-integrated ARPES measured dispersion with incident photon energy 9 eV (used for spin-resolved measurements). **b,** Spin-integrated Fermi surface mapping of Zn-Bi$_2$Se$_3$ at the native chemical potential (E$_B$ = 0.0 eV) **c,** Out-of-plane spin-resolved EDC spectra. **d,** Out-of-plane spin polarization obtained from **c.**

SI V. Ultra-thin undoped Bi$_2$Se$_3$

1. SR-APRES measurements, 3 QL vs 60 QL

Here we show the spin polarization measurements on 3 QL undoped Bi$_2$Se$_3$ (Fig. 4e-h in the maintext) again, and comparing the results with the spin polarization measurements on 60 QL undoped Bi$_2$Se$_3$. The thickness of 60 QL is well-above the quantum tunneling thickness limit. Thus no tunneling or coupling effect between the top and bottom surfaces is expected. This can also be seen from the ARPES measured *gapless* dispersion, as shown in Fig. S19c. The 3 QL and 60 QL SR measurements are performed with identical experimental conditions, except the film thickness. As shown in Fig. S19d, no reduction of the spin polarization is observed on 60 QL film surface, even at small momentum such as ± 0.03 Å^{-1}. Such measurements demonstrate the momentum resolution of the instruments, and show that the reduction of spin
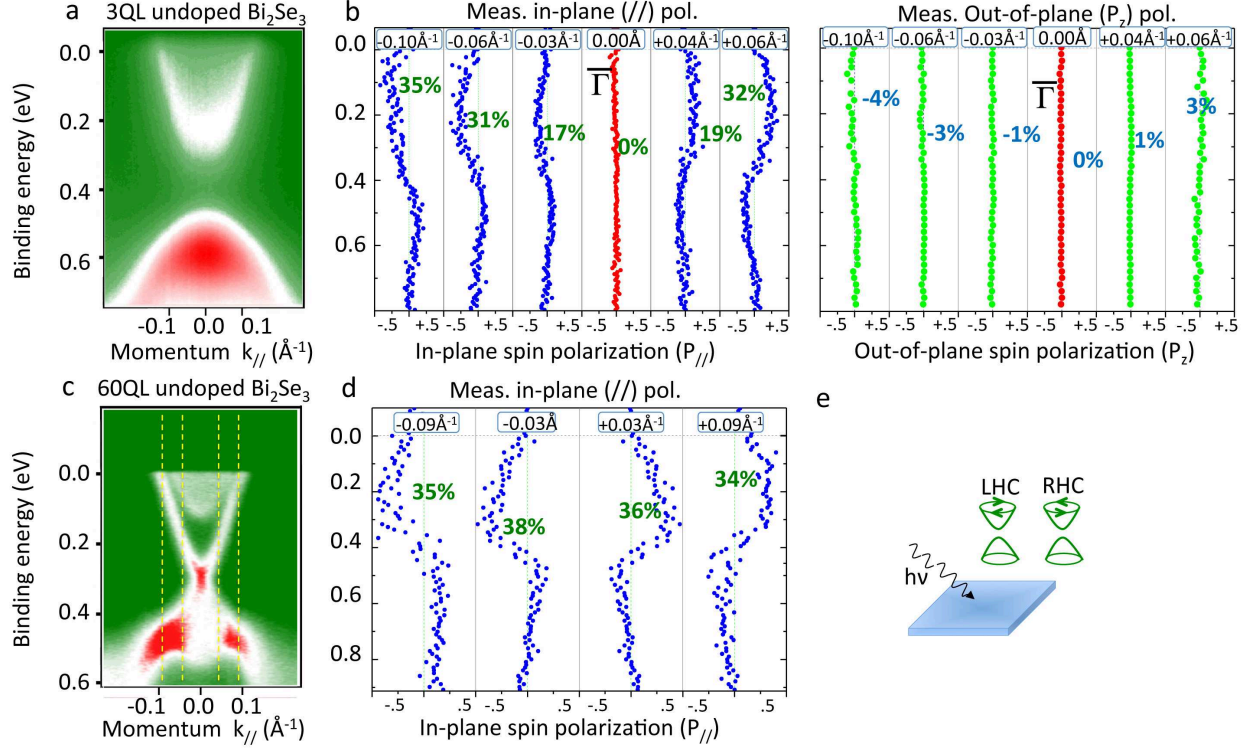
31

FIG. S19: **SR-APRES measurements, 3 QL vs 60 QL, demonstrating the momentum resolution of the instrument. a-b,** SR-ARPES measurements ($h\nu = 60$ eV) on 3 QL undoped Bi$_2$Se$_3$ shows reduction of spin polarization due at small momenta near the gap. Out-of-plane spin polarization does not show any significant spin polarization P$_z$, especially at the vicinity of the $\bar{\Gamma}$ momenta. **c-d,** SR-ARPES measurements on 60 QL undoped Bi$_2$Se$_3$ measured with identical experimental settings ($h\nu = 60$ eV) does not show any reduction of spin polarization. **e,** in 3 QL ultra-thin film, the surfaces from top and bottom are quantum mechanically coupled to each other, resulting in a tunneling gap as observed in panel **a**.

polarization on 3 QL film surface is not caused by blurring between the two branches of the upper Dirac cone due to the momentum resolution of the instrument.

SI VI. Spin-integrated ARPES dispersion fitting methods

Here we explain the method used to obtained the surface scattering analysis and the spectra weight suppression energy scale at the Dirac point in the maintext using the spin-

integrated ARPES dispersion mappings.
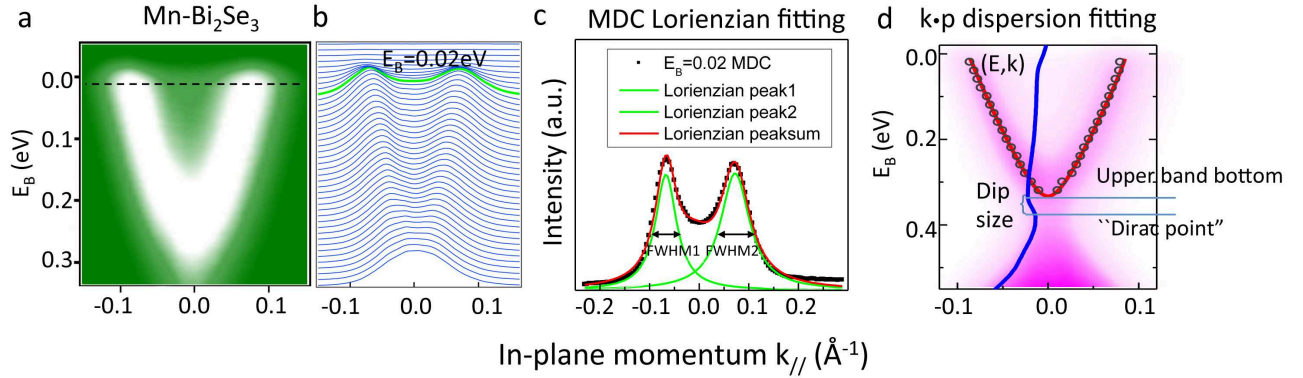
1. Momentum width

FIG. S20: **ARPES dispersion fitting methods. a-b,** Spin-integrated ARPES measured dispersion and MDCs on Mn-Bi$_2$Se$_3$ with incident photon energy 52 eV. The E$_B$ = 0.02 eV MDC is highlighted as an example to show the MDC Lorienzian fitting method. **c,** Lorienzian fitting of the MDC at E$_B$ = 0.02 eV. **d,** Dispersion fitting using $k \cdot p$ model [34] from the ARPES (E, k) obtained from **c.**

Recall the uncertainty principle from quantum mechanics, $\Delta k \cdot \Delta x \sim \hbar/2$. Thus, surface scattering can be evaluated from the inverse momentum width of the ARPES spectrum. We take the Mn-Bi$_2$Se$_3$ as example.

As shown in Fig. S20a-c, the MDC can be nicely fitted by a two-peak-Lorienzian profile. For the MDC at E$_B$ = 0.02 eV, the full width half maximum (FWHM) of the two Lorienzian peaks are 0.055 Å^{-1} and 0.071 Å^{-1}, respectively. Then the inverse momentum width Δk is given by: $1/\overline{FWHM}$, as shown in Fig. 2c in the maintext for different dopants and doping concentrations. We choose the FWHM at the Fermi level (E$_B$ = 0.02 eV), since it is more relevant to scattering of the electrons on the surface.

2. $k \cdot p$ dispersion fitting

Now we show how to fit the dispersion and obtain the energy scale of the spectra weight suppression (intensity dip) at the Dirac point, again using the example of Mn-Bi$_2$Se$_3$, From the Lorienzian fitting of the MDC (Fig. S20c), we can get the peak position of

33

the Lorienzian peak. From fitting the MDCs at all different binding energies, then the dispersion data points (E, k) can be extracted using ARPES dispersion measurements, which are shown by the grey circles in Fig. S20d.

We take the $k \cdot p$ Hamiltonian:

$$H = vk_{//}\sigma_{//} + mk_{//}^2 + H_z\sigma_z + o(k_{//}^3) + E_F \qquad (S11)$$

where E_F is a constant energy shift because in ARPES measurements $E = 0$ is at the native Fermi level rather than the Dirac point. The higher order $o(k_{//}^3)$ relevant to the Fermi surface warping is neglected since the Fermi surface is nearly isotropic in Bi_2Se_3. The energy spectrum (eigenvalue) can be obtained by solving the Schrödinger equation. For the upper Dirac band, we have:

$$E = \sqrt{(vk)^2 + (H_z)^2} + mk^2 + E_F \qquad (S12)$$

We fit the ARPES dispersion data points (E, k) (grey circles in Fig. S20d) with the $k \cdot p$ dispersion (red line in Fig. S20d). For Mn-Bi_2Se_3 (Mn=2.5%), we obtain $v = 2.5 \pm 0.7$ eVÅ^{-1}, $H_z = 0.057 \pm 0.03$ eV, $m = 0.097 \pm 0.025$ eVÅ^{-2} and $E_F = 0.39 \pm 0.03$ eV. Similar, e.g. for undoped Bi_2Se_3, we obtain $v = 2.2 \pm 0.4$ eVÅ^{-1}, $H_z = 2 \times 10^{-4}$ eV, $m = 0.113 \pm 0.010$ eVÅ^{-2} and $E_F = 0.40 \pm 0.02$ eV. We list the fitted parameter values as follows:

Nominal concentration	v (ev·Å^{-1})	m(ev·Å^{-2})	E_F(eV)	H_z(eV)
Undoped	2.2±0.4	0.113±0.010	0.40±0.02	0.0002±0.01
Mn(1.0%)	2.3±0.4	0.0126±0.020	0.42±0.04	0.023±0.01
Mn(2.5%)	2.5±0.7	0.097±0.025	0.39±0.03	0.057±0.03
Mn(10%)	3.1±1.5	0.234±0.124	0.33±0.14	0.087±0.06
Zn(0.5%)	2.6±0.4	0.123±0.009	0.38±0.03	0.003±0.02
Zn(1.5%)	2.5±0.6	0.156±0.045	0.37±0.05	0.004±0.02
Zn(10%)	2.4±0.7	0.124±0.056	0.33±0.06	0.009±0.04

FIG. S21:

We would like to point out that the H_z in this section is obtained from fitting the spin-integrated ARPES dispersion. Therefore, the H_z here is more relevant to the energy scale of the spectra weight suppression at the Dirac point E_{SWS} in the maintext. In Fig. 5 of the maintext, we obtain the magnetic interaction strength b_z from the spin-resolved measurements. In the ideal magnetic scenario, where the spectra weight suppression can only be caused by the magnetic contribution, b_z, H_z and E_{SWS} are equivalent. However, since SWS can also be induced by TR invariant factors, the magnetic contribution can only be isolated by spin-resolved measurements.

35

[1] Balasubramanian T. *et al.* The Normal Incidence Monochromator Beamline I3 on MAX III. *AIP Conf. Proc.* **1234**, 661-664 (2010).

[2] Berntsen M. H. *et al.* A spin- and angle-resolving photoelectron spectrometer. *Rev. Sci. Instrum.* **81**, 035104 (2010).

[3] Hoesch M. *et al.* Spin-polarized Fermi surface mapping. *J. Electron Spectrosc. Relat. Phenom.* **124**, 263-279 (2002).

[4] Meier F. *et al.* Quantitative vectorial spin analysis in angle-resolved photoemission: Bi/Ag(111) and Pb/Ag(111). *Phys. Rev. B* **77**, 165431 (2008).

[5] Dil, J. H. Spin and angle resolved photoemission on non-magnetic low-dimensional systems. *J. Phys. Condens. Matter* **21**, 403001 (2009).

[6] Perdew, J. P., Burke K. & Ernzerhof M., Generalized Gradient Approximation Made Simple. *Phys. Rev. Lett.* **77**, 3865 (1996).

[7] Kresse G. & J. Joubert, From ultrasoft pseudopotentials to the projector augmented-wave method. *Phys. Rev. B* **59**, 1758 (1999).

[8] Kress G. & Furthmuller J., Efficient iterative schemes for ab initio total-energy calculations using a plane-wave basis set. *Phys. Rev. B* **54**, 11169 (1996).

[9] Hsieh D. *et al.* A tunable topological insulator in the spin helical Dirac transport regime. *Nature* **460**, 1101-1105 (2009).

[10] Zhu J.-J. *et al.* Electrically Controllable Surface Magnetism on the Surface of Topological Insulators. *Phys. Rev. Lett.* **106**, 097201 (2011).

[11] Chen Y.-L. *et al.* Massive Dirac Fermion on the Surface of a Magnetically Doped Topological Insulator. *Science* **329**, 659-662 (2010).

[12] Zhang D. *et al.* In submission (2012). Both SIMS and STM measurements are in private communication.

[13] Zhao L. X. *et al.* Intrinsic and extrinsic contributions to the lattice parameter of GaMnAs. *Appl. Phys. Lett.* **86**, 071902 (2005).

[14] Stohr J., Exploring the microscopic origin of magnetic anisotropies with X-ray magnetic circular dichroism (XMCD) spectroscopy. *J. Magn. Magn. Mater.* **200**, 470-497 (1999).

[15] Stohr J., X-ray magnetic circular dichroism spectroscopy of transition metal thin films. *J.*

Electron Spectrosc. Relat. Phenom. **75**, 253-272 (1995).

[16] Edmonds K. W. *et al.* Secondary magnetic phases in (Ga,Mn)As determined by x-ray magnetic circular dichroism. *J. Appl. Phys.* **102**, 023902 (2007).

[17] Okabayashi J. *et al.* Electronic and magnetic properties of MnAs nanoclusters studied by x-ray absorption spectroscopy and x-ray magnetic circular dichroism. *Appl. Phys. Lett.* **83**, 5485 (2003).

[18] Chen C. T. *et al.* Experimental Confirmation of the X-Ray Magnetic Circular Dichroism Sum Rules for Iron and Cobalt. *Phys. Rev. Lett.* **75**, 152 (1995).

[19] Jungwirth T. *et al.* Low-temperature magnetization of (Ga,Mn)As semiconductors. *Phys. Rev. B* **73**, 165205 (2006).

[20] Hor, Y. S. *et al.* Development of ferromagnetism in the doped topological insulator $Bi_{2-x}Mn_xTe_3$. *Phys. Rev. B* **81**, 195203 (2010).

[21] Liu, M. *et al.* Crossover between weak localization and weak antilocalization in magnetically doped topological insulator. *Phys. Rev. Lett.* **108** 036805 (2012).

[22] Vobornik, I. *et al.* Magnetic Proximity Effect as a Pathway to Spintronic Applications of Topological Insulators. *Nano Lett.* **11**, 4079-4082 (2011).

[23] Qi, X.-L., Hughes, T. L. & Zhang, S.-C. Topological field theory of TR invariant insulators. *Phys. Rev. B* **78**, 195424 (2008).

[24] Garate, I. & Franz, M. Inverse spin-galvanic effect in the interface between a topological insulator and a ferromagnet. *Phys. Rev. Lett.* **104**, 146802 (2010).

[25] Yu, R. *et al.* Quantized anomalous Hall effect in magnetic topological insulators. *Science* **329**, 61-64 (2010).

[26] Qi, X.-L. *et al.* Inducing a magnetic monopole with topological surface states. *Science* **323**, 1184-1187 (2009).

[27] Wray, L. A. *et al.* A topological insulator surface under strong Coulomb, magnetic and disorder perturbations. *Nature Phys.* **7**, 32-37 (2011).

[28] Okada, Y. *et al.* Direct Observation of Broken Time-Reversal Symmetry on the Surface of a Magnetically Doped Topological Insulator. *Phys. Rev. Lett.* **206805**, (2011).

[29] Sato T. *et al.* Unexpected mass acquisition of Dirac fermions at the quantum phase transition of a topological insulator. *Nature Phys.* **7** 840-844 (2011).

[30] Beidenkopf, H. *et al.* Spatial fluctuations of helical Dirac fermions on the surface of topological

insulators. *Nature Phys.* **7**, 939-943 (2011).

[31] Bergman, D. L. & Refael, G. Bulk metals with helical surface states. *Phys. Rev. B* **82**, 195417 (2010).

[32] King, P. D. C. *et al.* Large Tunable Rashba Spin Splitting of a Two-Dimensional Electron Gas in Bi_2Se_3. *Phys. Rev. Lett.* **107** 096802 (2011).

[33] Wray L. A. *et al.* In submission. (2011).

[34] Fu, L. *Phys. Rev. Lett.* **103**, 266801 (2009).

Correspondence and requests for materials should be addressed to M.Z.H. (Email: mzhasan@princeton.edu).